Infrared Spectroscopy and Mass Spectrometry of CO2 Clusters during Nucleation and Growth

Infrared Sectroscopy and Mass Spectrometry of CO_2 Clusters during Nucleation and Growth

Martina Lippe, Urszula Szczepaniak, Gao-Lei Hou, Satrajit Chakrabarty, Jorge J. Ferreiro, Egor Chasovskikh, and Ruth Signorell*

Laboratory of Physical Chemistry, ETH Zürich, Vladimir-Prelog Weg 2, CH-8093 Zürich, Switzerland

submitted to

J. Phys. Chem. A

March 2, 2019

*corresponding author: rsignorell@ethz.ch, Tel: +41 44 633 46 21, Fax: +41 44 633 13 16

Abstract

CO_2 clusters with 2 to 4300 molecules are characterized with mass spectrometry and infrared spectroscopy in the uniform postnozzle flow of Laval expansions at constant temperatures of $\sim 29\,\mathrm{K}$ and $\sim 43\,\mathrm{K}$. The mass spectra provide independent, accurate information on the cluster size distributions and through magic numbers also on cluster structures. The experimental results are complemented with force field, quantum chemical, and vibrational exciton calculations. We find our data to be consistent with predominantly fcc cuboctahedral structures for clusters with more than about 50 molecules. Infrared spectra of cluster size distributions with average sizes above 140-220 molecules are completely dominated by the features from the larger cuboctahedral clusters in the distribution. For very small clusters, exciton simulations predict a pronounced broadening of the infrared band as soon as the average cluster size exceeds about 5 molecules. The nucleation behavior of CO_2 under the present conditions is found to be barrierless in agreement with similar trends previously observed for other compounds at very high supersaturation.

1 Introduction

Weakly bound molecular aggregates play an important role in atmospheric processes not only in the Earth's atmosphere but also in other planetary atmospheres. This includes their role in the very first steps of aerosol and cloud formation; i. e. in nucleation and early growth processes; which are still rather poorly understood. In the Martian atmosphere, CO_2 clouds are the equivalent of H_2O clouds on Earth[1,2,3,4]. In laboratory studies, many different techniques have been used to generate and characterize weakly bound molecular aggregates, also with the aim to learn more about nucleation and early cluster growth. Infrared spectroscopy has proven to be particularly useful in this context, not only providing structural information on small clusters but also on the phase and morphology of very large aggregates. Small oligomers are typically generated in free supersonic or slit nozzle expansions and characterized with high resolution infrared or Fourier transform infrared (FTIR) spectroscopy (see refs.[5,6,7,8,9,10,11,12,13,14,15,16,17] and references therein). An independent determination of the cluster size is usually not necessary for the very small clusters because the infrared spectra change pronouncedly from cluster size to cluster size thus enabling unambiguous assignments. Very large aggregates, containing billions of molecules, have been studied in collisional cooling cells with FTIR spectroscopy[1,18,19,20,21,22,23,24,25,26,27,28]. In this size range, the features in the infrared spectra are almost insensitive to the aggregate size so that sizing does not pose a particular issue here[29,30,31,32]. The formation of aggregates with less than $\sim 10^4$ molecules, however, is very challenging in collisional cooling cells, so that this size range usually remains unexplored. Laval expansions in combination with FTIR spectroscopy provide a mean to bridge the gap between infrared studies of small oligomers and those performed in collisional cooling cells on very large aggregates[33,34,35,36,37,38,39]. When the expansion is probed with infrared spectroscopy in the uniform postnozzle flow[34,39] it has the additional advantage that the cluster temperature is well-known, similar to collisional cooling cells. This is not the case in free supersonic or slit nozzle expansions where clusters are not probed under thermal equilibrium conditions. However, the issue in the intermediate cluster size range accessible by Laval expansions is the determination of the cluster size

distribution. Here, an independent accurate method for cluster sizing is essential because the expansions produce broad size distributions and the infrared spectra are strongly size-dependent.

To account for this, the present work combines Laval nozzle expansions with FTIR spectroscopy and mass spectrometry, both of which probe the expansion in the uniform postnozzle flow. For CO_2 aggregates, mass spectrometry offers several advantages. Firstly, through the exact mass it provides information on the cluster size distribution; i. e. on the mass and the relative abundance of clusters; and for each size on the number of molecules per cluster. Secondly, magic number clusters appear in the mass spectra and provide information on the cluster structure through geometrical analysis[40,41,42]. It has been shown in previous studies through the observation of so-called shell and subshell closings that CO_2 clusters with more than about 25-55 molecules form cuboctahedral shapes with an fcc crystal structure[40,41,42,43,44,45]. Furthermore, CO_2 clusters show very distinct features in the mid-infrared region due to strong dipole coupling between the different CO_2 molecules in the clusters, which is also referred to as vibrational exciton coupling[31,46]. As a consequence of the dominant dipole coupling, vibrational bands are unusually sensitive to the internal structure and the morphology of the clusters. Here, we focus on the asymmetric stretching band of the CO_2 clusters because it is the strongest vibrational band with the biggest effects from exciton coupling. The experimental results are complemented by vibrational exciton calculations, for which we use the information on the cluster size distribution and cluster structure from mass spectrometry. The mass spectra cannot provide structural information for clusters with less than about 55 molecules. In this size range, we use force field (FF) and density functional (DFT) calculations for the determination of the cluster structures.

2 Experiment

Except for the infrared part, the experimental setup (Fig. 1) has been described in detail in previous publications[47,48,49,50,51]. CO_2 clusters are generated in pulsed Laval

expansions and characterized in the uniform postnozzle flow by mass spectrometry and Fourier transform infrared spectroscopy (FTIR). We use mass flow controllers to regulate the flow of the carrier gas Ar (PanGas, 5.0) and the condensable gas CO_2 (PanGas, 4.5). For the nucleation measurements, we add small amounts of CH_4 (Messer Schweiz, 5.5) to the carrier gas in order to change the flow temperature slightly and thus the supersaturation in fine steps (see section 4.1). The gas mixture is supplied to the stagnation volume (stagnation pressure p_0, stagnation temperature T_0) by two feeding valves (not shown). The opening times of the valves are 6 ms and 41 ms for the mass spectrometric and the infrared spectroscopic measurements, respectively. From the stagnation volume, the gas mixture is then expanded through the Laval nozzle into the first vacuum chamber. The Laval nozzle generates a uniform flow at the nozzle exit, which is extended into the postnozzle flow region by matching the pressure in the first vacuum chamber to the flow pressure p_F. The impact pressure p_I is measured as a function of the axial distance l with pressure transducers. The flow temperature T_F is determined from p_0 and p_I using the Rayleigh-Pitot relation, and assuming isentropic relations and ideal gas behavior[50,51,52]. In this work, we use two Laval nozzles with flow pressures p_F of 35 Pa and 33 Pa, respectively, and axially averaged flow temperatures of $\overline{T}_F$ of 29.4 ± 1.2 K and 42.6 ± 1.6 K, respectively. An additional Laval nozzle with $\overline{T}_F = 47.5 \pm 1.2$ K and $p_F = 40$ Pa is used to record the gas phase spectra (CO_2 concentration 7%) in Figs. 4, 8a, 10a and 11a. The Laval nozzle is mounted on a translation stage so that the axial distance l can be changed in steps as small as 1 mm over the whole range of the stable postnozzle flow of $l_{max} =$ 100 mm. This allows us to observe the temporal cluster evolution over a time scale of $\sim$ 200 μs with a temporal resolution of $\sim 2\,\mu$s. The fixed positions of both the mass and the infrared spectrometers required to perform two consecutive measurements to ensure that the same region of the postnozzle flow is probed with both methods. For that purpose, the Laval nozzle is moved between the two measurements so that the distance of the nozzle exit to the infrared beam is identical to the distance of the nozzle exit to the skimmer of the mass spectrometer. In other words, for the infrared measurements the axial distance l is the nozzle exit to infrared beam distance, while for the mass spectrometric

studies l corresponds to the nozzle exit to skimmer distance (see Fig. 1).

For the mass spectrometric measurements, the central part of the Laval expansion is sampled by a skimmer (1 mm diameter) into the mass spectrometer, where the neutral clusters are ionized just above the first ionization threshold by single vacuum ultraviolet (VUV) photons from a home-built, low fluence table top VUV laser[47,48,49,53]. It has been shown that this ionization method is a comparatively soft ionization method even for weakly bound clusters[54,55,56,57,58]. The VUV light is generated by resonance-enhanced two-color four-wave mixing in a Kr gas expansion at 20 Hz[50,53]. We use a photon energy of 13.8 eV (89.8 nm) which is close to the ionization threshold of CO_2 monomer (13.778 eV,[59]). The photon flux is on the order of $\sim 10^{11}$-10^{12} photons/(cm^{2}pulse). The ions are then accelerated by a Wiley McLaren type mass spectrometer and detected by a multichannel plate (MCP) detector. We use high extraction voltages up to 30 kV to achieve high sensitivity. In addition, for the cluster studies the monomer ion is selectively deflected by a pulsed electric field applied to a plate located in front of the MCP detector to avoid saturation effects [48,50,51].

The infrared measurements are performed with a Bruker IFS 66v/s FTIR spectrometer and a liquid nitrogen cooled HgCdTe (MCT) detector. The spectrometer, the infrared beam path, and the detector chamber are evacuated to $\sim$ 7 mbar and are connected to the first vacuum chamber with two KBr windows (see Fig. 1). The infrared beam is focused onto the center of the Laval expansion to maximize the signal from the clusters located in the cold core of the Laval expansion. The pathlength (distance between the two KBr windows) is $\sim$ 350 mm and the width of the Laval expansion (cluster region) is $\sim$ 10 mm. For the infrared measurements, the pulsed feeding valves are triggered by the FTIR spectrometer. The opening times of the pulsed valves is increased to 41 ms to match the minimum time required for recording an interferogram in the steady state region of the pulsed Laval expansion, and the repetition rate was set to 10 Hz. Note that the flow conditions remain identical to those for the mass spectrometric measurements. The measurements are performed with the RapidScan option with a spectral resolution of 1.5 cm^{-1}. Typically, 9600 interferograms are averaged and then Fourier transformed.

The spectra are then converted to absorbance spectra using spectra of the empty chamber as background.

The combination of low spectral resolution ($1.5\,\mathrm{cm}^{-1}$) and low gas pressures ($<$ 1 mbar) in the vacuum chamber leads to pronounced artifacts in the CO_2 gas phase infrared spectra. This is exemplified in Fig. 2. The intrinsic line widths of the rotational transitions of gaseous CO_2 are very narrow. Therefore, if spectra are recorded at low total gas pressure, as in our Laval expansions ($<$ 1 mbar), with low spectral resolution this results in false relative intensities of the different rotational transitions in the CO_2 gas phase spectra. Two examples for spectral resolutions of $1.5\,\mathrm{cm}^{-1}$ and $0.25\,\mathrm{cm}^{-1}$ are shown in the top part of Fig. 2. Neither of these two spectra shows the correct intensity distribution of gaseous CO_2. As the bottom part shows, pressure broadening removes these artifacts when the total pressure is increased to about 1 bar by addition of Ar gas. The maximum resolution and the maximum pressure in the Laval expansion cannot be increased beyond $1.5\,\mathrm{cm}^{-1}$ and above 1 mbar (top black trace in Fig. 2) so that the gas phase artifacts cannot be avoided. As a result of the limited resolution, subtraction of gas phase contributions is difficult and (residual) gas phase contributions cannot be easily distinguished from the broad cluster features.

3 Calculations

3.1 FF and DFT calculations

For the force field (FF) calculations, the artificial bee colony (ABC) algorithm is employed by using the ABCluster 1.5 program to generate hundreds to thousands of low energy isomers of $(CO_2)_n$ clusters with n up to 600[60,61]. The CHARMM force field[62] is used for the CO_2 molecule (see Table S1 in in the Supporting Information). The structure of the 15 energetically lowest lying isomers for each cluster size up to $n = 38$ is further optimized with density functional theory (DFT). All DFT computations were performed with the Gaussian09 program package[63]. Three functionals - B3LYP[64,65,66], B2PLYP-D[67], and M06-2X[68] - are tested for n = 1-4 (see Table S2 in in the Supporting

Information). Pople's 6-31+G(d) basis set is used for all the atoms up to $n = 25$ and 6-31G(d) for larger clusters up to $n = 38$[69]. We found the three functionals to result in minimum structures with essentially the same structural characteristics. This is in agreement with the findings of previous studies[70,71]. Furthermore, Lemke et al.[70] showed that for $(CO_2)_n$ clusters with n up to 16, the M06-2X functional provides reliable results compared with benchmark calculations at the CCSD(T) level of theory. Therefore, the M06-2X functional is used here for larger clusters up to $n = 38$. All structures are optimized without any symmetry constraint. Harmonic vibrational frequencies are calculated to confirm that the optimized structures are real minima, and to simulate infrared spectra of the clusters for comparison with vibrational exciton calculations (see next subsection). In most cases, the most stable isomer generated from the FF search is also the most stable one after optimization at the M06-2X/6-31+G(d) level. The main change of the structures upon optimization is an overall decrease of the intermolecular distances in the cluster with additional rotations of some specific CO_2 molecules in the cluster. Based on these results, we use the lowest energy structure from FF calculations also for the clusters with n = 39-50, for which DFT/M06-2X optimization is computationally too expensive. We also considered the minimum structures of small $(CO_2)_n$ clusters studied in refs.[44,72]. The global minimum structures identified in our study are either the same or more stable structures compared with this previous investigation.

The C=O bond distance of linear CO_2 is optimized to be 1.163 Å, which is in excellent agreement with the experimental value of 1.162 Å[73]. The antisymmetric stretching mode (ν_3) of CO_2 is calculated to be 2468 cm^{-1}. To match the experimentally measured ν_3 of 2349 cm^{-1}[74], a scaling factor of 0.9518 has to be applied. This scaling factor is also used to scale the calculated vibrational frequencies of clusters with n = 2-25 in the ν_3 region, while for clusters with n = 26-38 a scaling factor of 0.9450 is employed. The latter corrects for the difference between vibrational frequencies of $(CO_2)_{25}$ calculated with the 6-31G(d) and 6-31+G(d) basis sets using the M06-2X functional. Note that we do not use different scaling factors for clusters $(CO_2)_n$ with n = 2-13, for which high resolution IR spectroscopy measurements are available[5,6,7,75,76,77,78]. Rather, we focus on the general

trends of the infrared band shapes as a function of cluster size. Structures and infrared spectra for the obtained isomers for $(CO_2)_n$ clusters with n = 2-4 are provided in Figs. S1 and S2 in the Supporting Information. Figs. S3 and S4 in the Supporting Information present the optimized most stable structures of $(CO_2)_n$ for n = 5-38 from M06-2X and selected structures for n = 40-600 from the FF calculations, respectively. The Cartesian coordinates of the energetically lowest lying isomers for n = 2-38 and n = 40, 45, and 50 are provided in Table S3. Note that the second most stable structures are typically about 2-4 kJ/mol higher in energy than the most stable ones using the M06-2X method.

3.2 Vibrational exciton calculations

We have previously shown that infrared spectra of CO_2 clusters are dominated by contributions from resonant dipole coupling and can thus be reliably simulated using vibrational exciton calculations[31,46,79]. The resonant dipole coupling term is dominant for molecular systems with strong molecular transition dipole moments ($>$ 0.1-0.2 D) and small intermolecular distances ($<$ 5-7 Å). The transition dipole moment of CO_2 in the region of the antisymmetric stretching vibration (ν_3 band) is on the order of 0.32 D[79,80] and the intermolecular distances in the clusters are in the range of 3-4 Å[31,78]. The vibrational Hamiltonian $\hat{H}$ can be written as[31,79,81]:

$$\hat{H} = \hat{H}_0 + \hat{H}_{\mathrm{D}} \tag{1}$$

$\hat{H}_0$ is the sum over the vibrational Hamiltonians of the uncoupled molecules and $\hat{H}_{\mathrm{D}}$ includes all pairwise dipole-dipole interactions between molecules in the cluster. $\hat{H}_{\mathrm{D}}$ is given by:

$$\hat{H_{\mathrm{D}}} = \sum_{i<j} -\frac{1}{4\pi\epsilon_0}\overrightarrow{\mu_i}\frac{3(\overrightarrow{\mu_j}\cdot\overrightarrow{r_{ij}})\cdot\overrightarrow{r_{ij}} - (\overrightarrow{r_{ij}}\cdot\overrightarrow{r_{ij}})\cdot\overrightarrow{\mu_j}}{\overrightarrow{r_{ij}}^5} \tag{2}$$

$\overrightarrow{r_{ij}}$ is the displacement vector between the centers of mass of the two molecules i and j and $\overrightarrow{\mu}$ is the dipole moment operator. Up to first order terms in the vibrational coordinates, the model contains only two input parameters in addition to the cluster structure, which are the transition wavenumber of the uncoupled molecule $\tilde{\nu}_{\mathrm{M}}$ and the molecular transition

dipole moment $\delta\mu = \langle 0|\mu|1\rangle$. For the present calculations, we use $\tilde{\nu_{\mathrm{M}}} = 2355\,\mathrm{cm}^{-1}$ and $\langle 0|\mu|1\rangle = 0.32\,\mathrm{D}$[46]. The vibrational eigenvalues and eigenfunctions of the cluster are obtained by diagonalization of $\hat{H}$ or through calculation of the autocorrelation function of the dipole moment[22,31,79]. For the cluster structures, we use the energetically lowest lying structures as obtained from the FF after further optimization with DFT for n = 2-38, while in the size range n = 39-50 we directly use the energetically lowest lying structures from FF calculations. All larger clusters were modeled as cuboctahedral structures with fcc crystal structure in agreement with the results from previous studies[40,41,43,44,45,72,82]. For this purpose, an fcc crystal structure is constructed by copying a CO_2 unit cell in three directions, from which molecules are removed until a perfect cuboctahedron was obtained. These so-called closed shell cuboctahedra have only very distinct sizes. To model clusters with size between these special closed shell structures, we remove molecules from faces. The removal of complete faces result in subshell closed cuboctahedra. We refer to all these structures simply as fcc cuboctahedral structures.

The reliability of the exciton approach for CO_2 clusters was verified in our previous publications[31,46,79]. Here, we add a more extensive comparison with quantum chemical calculations for the cluster size range n = 2-38 (Fig. 3 and Fig. S5 in the Supporting Information). Fig. 3 shows selected results for n = 13, 19, 28 and 38. The top (black) and the bottom (red) trace are infrared spectra calculated with the exciton approach and with DFT, respectively. The same cluster structures as obtained from optimization with DFT at the M06-2X level of theory are used as input structures for both vibrational calculations. The similar infrared band shapes verify that resonant dipole coupling is able to capture the main features in the infrared spectra (see also Fig. S5 for more data). This is an important result because the exciton approach is the only method that can be applied to even larger clusters containing many thousands of molecules. We mentioned above that the optimization of the FF generated structures with DFT mainly results in a decrease of the intermolecular distances of the molecules in the clusters. To evaluate the influence of this decrease on the infrared spectra we show in the middle (blue) trace of Fig. 3 infrared spectra calculated with the exciton model but this time for FF structures

without further optimization by DFT. The agreement with the exciton spectra in the top (black) trace is very good. The shorter intermolecular distances after DFT optimization results in a slightly stronger dipole coupling, which explains the slightly broader overall band width of the spectra in the top trace. This comparison mainly confirms that our approach to use DFT optimized structures for $n < 39$ and FF structures for $n = 39$-50 has almost no effect on the infrared spectra. Based on the favorable comparisons in Fig. 3 and Fig. S5 in the Supporting Information, we will use throughout the remainder of this work exclusively exciton calculation for the modeling of infrared spectra for all cluster sizes. The cluster sizes and the relative abundances of different cluster sizes will be taken from the experimental mass spectra, and as mentioned above we will use DFT optimized structures for $n < 39$, FF structures for $n = 39$-50, and fcc cuboctahedral structures for larger clusters.

4 Results and discussion

4.1 Small clusters and nucleation

We have recently shown that mass spectrometry in the uniform postnozzle flow of a Laval nozzle allows one to capture the very first steps of gas phase nucleation/condensation at the molecular level[47,48,49]. Infrared spectroscopy could provide additional information on cluster structures in this size range, where the average cluster size $< n >$ and the maximal cluster size $n_{\max}$ typically lie below about ten and a few ten molecules, respectively. The thermodynamic requirement for nucleation to take place is that the supersaturation S is larger than 1, where $S = \frac{p_{\mathrm{cond}}}{p_{\mathrm{eq}(T_{\mathrm{F}})}}$ with the partial pressure of the condensable (here CO_2) p_{cond} and the equilibrium vapor pressure of the condensable $p_{\mathrm{eq}(T_{\mathrm{F}})}$ at the flow temperature T_{F}. However, nucleation can only be observed if it occurs in the time window that is accessible by a given experiment. As explained in refs.[47,48,49], we thus refer to conditions where $S > 1$ but nucleation can not yet be observed as *subcritical*, and conditions at which nucleation just becomes observable as *supercritical*. The first steps of nucleation/condensation can then be followed by tuning the conditions in very fine

steps from subcritical to supercritical conditions. In the present work this tuning was achieved by adding small amounts of methane gas (maximum of less than 10%) to the argon carrier gas while recording infrared and mass spectra at a constant axial distance. Successive addition of methane gas results in very small ($< 0.5\,\mathrm{K}$) increases of T_F, which in turn results in a continuous decrease of the average and maximum cluster sizes until nucleation/condensation is completely inhibited [47,48,49].

The middle and the lower traces in Fig. 4 show two example infrared spectra recorded at methane concentrations of 5% and 2.46%, respectively, which correspond to maximum cluster sizes of $n_\mathrm{max} = 21$ and $n_\mathrm{max} = 33$, respectively (see mass spectra in Fig. 5b). Surprisingly, the two spectra look identical even though the cluster sizes differ substantially. This also holds for infrared spectra (not shown) recorded at the other methane concentrations/cluster sizes (see mass spectra in Fig. 5b). For such small clusters one expects substantially different infrared spectra for different cluster sizes; i. e. just the opposite of the experimental results. The observed independence of the infrared spectra from the cluster size can be explained by comparison with the pure gas phase spectrum in the upper trace of Fig. 4. It reveals that the cluster spectra are dominated by gas phase contributions to such an extent that no cluster features are visible. Under nucleation conditions, the cluster number concentrations lies ~ 3 orders of magnitude below the CO_2 monomer number concentration, which is on the order of $\sim 10^{14}\,\mathrm{cm}^{-3}$. Given the low infrared monomer signal (low signal-to-noise (S/N) ratio), it is thus not surprising that our infrared experiment is not sensitive enough to detect any cluster signals under these expansion conditions.

Even though we cannot record infrared spectra during the first steps of nucleation/condensation, Fig. 5b shows that the higher sensitivity of mass spectrometry allows us to observe the evolution of the cluster size distribution under these conditions. The maximal cluster sizes n_max indicated by black arrows vary over the ranges from about 5 to 38 molecules. Note that at methane concentrations higher than the ones used for the top spectrum in Fig. 5b only monomer is observed (subcritical conditions). The detailed experimental information of the cluster size distributions (size and relative abundance) together with

modeling (structure and exciton modeling, see section 3.2) allows us at least to predict the infrared spectra. As mentioned earlier, the transition to fcc cuboctahedral structure is expected in the region of $n \sim$ 25-55 molecules[40,41,42,44,43,45] so that we can safely assume that with an overall largest cluster size of $n_{\max} = 38$ the dominating cluster sizes do not yet have cuboctahedral structure. We thus used for each cluster size the structures of the energetically lowest lying isomer as predicted by the FF calculation and further optimized by DFT (see section 3.1). The corresponding modeling results are shown in Fig. 5a. The simulated infrared spectra show a pronounced increase by about a factor of four of the band width with increasing $n_{\max}$. This broadening can be explained as follows: in the cluster size range $n < 38$, both the geometrical structure and the infrared spectra of individual cluster sizes change drastically from one cluster size to another (see section 3.1). Therefore, the larger $n_{\max}$ becomes, the more different cluster sizes with different infrared spectra contribute to the overall infrared spectrum. We had already reported on infrared spectra of CO_2 clusters with average sizes of $< n > \leq 100$ in a previous study (see Fig. 5 in ref.[34]). However, for lack of an accurate sizing method the average size could only be estimated in that work to be likely below 100 without any further specification of the lower bound. The largest average cluster size in the present study is $< n >= 9$ (see bottom spectrum in Fig. 5b). The spectral differences (band widths and structures) between the present infrared spectra and the spectra in Fig. 5 of ref.[34] thus hint that the average size of the latter was above $< n > \sim 10$, finally providing a lower bound for the size estimate of those spectra.

In our previous papers on nucleation of water, toluene, and propane [47,48,49], we suggested that the type of nucleation behavior can be extracted from graphs showing $n_{\max}$ as a function of $\ln S$ (see for example Fig. 6a and Fig. 4 in ref.[47]). We found two types of nucleation behavior: a steplike and a gradual increase of the cluster size with increasing supersaturation. For water and propane a systematic trend from a steplike behavior at lower $\ln S$ to a gradual at higher $\ln S$ was found. A steplike increase of $n_{\max}$ with increasing $\ln S$ was considered to be indicative of the presence of a nucleation barrier, while a gradual increase was suggested to hint at a barrierless condensation process (spinodal

decomposition). Our recent study on water nucleation, however, challenges this simple interpretation, indicating that a steplike increase could also be caused by a kinetic bottleneck other than a free energy barrier[47]. The highest ln$S$ in all these previous studies was around 104. The current CO_2 data are recorded at an even higher ln$S$ around 150. Thus, from the previously observed trend one would clearly expect CO_2 condensation to take place in a barrierless regime; i. e. one would expect to observe a gradual increase of $n_{\max}$ with increasing ln$S$. Fig. 6a shows that this is indeed the case and CO_2 also seems to follow the trend observed for the other compounds. It also reveals that the critical supersaturation for CO_2 condensation under these conditions lies at ln$S \sim 138$. Cluster size distributions recorded as a function of ln$S$ at a constant nucleation/growth time (constant axial position in the postnozzle flow) provide information on the nucleation behavior (Fig. 6a) and on critical cluster sizes, which for barrierless condensation is the monomer. As described in detail in ref.[47], the nucleation/growth rate J can be extracted from the total cluster number concentration $N_{\mathrm{cluster,tot}}^{\mathrm{CO_2}}$ recorded as a function of the nucleation/growth time t, where t is varied by varying the axial distance in the postnozzle flow by fine steps. $N_{\mathrm{cluster,tot}}^{\mathrm{CO_2}}$ is the sum over all cluster number concentrations. Fig. 6b shows $N_{\mathrm{cluster,tot}}^{\mathrm{CO_2}}$ as a function of t for ln$S = 160$. At early nucleation times, monomer depletion and more complex growth processes (cluster agglomeration and coagulation) are negligible. At these early t, $N_{\mathrm{cluster,tot}}^{\mathrm{CO_2}}$ is proportional to t[47]. A linear fit to the data at early t predicts a value of $J \sim 1 - 2 \cdot 10^{15}\,\mathrm{cm^{-3}s^{-1}}$ at ln$S = 160$, which in the case of barrierless condensation is rather a growth than a nucleation rate in its usual sense[47]. To the best of our knowledge these are the first data for CO_2 condensation at such low temperatures ($\overline{T}_{\mathrm{F}} = 29.4 \pm 1.2\,\mathrm{K}$) and high supersaturations. The uncertainty of the nucleation rate constants are estimated to be one order of magnitude (for more information see[47]). CO_2 nucleation rates have previously been determined to lie in the range $J \sim 10^{17} - 10^{21}\,\mathrm{cm^{-3}s^{-1}}$ at a supersaturation of $S \sim 10$ and temperatures of 160-190 K[83]. These experiments were also performed in Laval nozzles. However, in contrast to our case condensation most likely takes place in the presence of a nucleation barrier under the conditions of ref.[83].

4.2 Intermediate cluster sizes

In this section, we present infrared and mass spectra of intermediate cluster sizes, which cover the average cluster size range from $< n >\sim$ 20-330 ($n_{\max} \sim$ 70-710). This coincides with the size range where the transition to fcc cuboctahedral structures takes place around $n \sim$ 25-55[40,41,42,43,44,45]. The appearance of fcc cuboctahedral clusters is exemplified in the mass spectrum in Fig. 7. For cluster sizes with $n \gtrsim 55$, different minima are observed in the mass spectra, which are labeled with asterisks in the inset in the figure. Such patterns were observed for different substances; e. g. CO_2, SF_6, and rare gases; and were attributed to shell and subshell closings[40,41,42]. These cluster sizes correspond to particularly stable cluster structures (magic clusters), which in the case of CO_2 appear as local minima in the mass spectra because of their lower ionization efficiency. Note that as a consequence of the latter, the relative abundances of these clusters is underestimated from the ion signals in the mass spectra. We have confirmed the cuboctahedral structure of these special clusters for all mass spectra following the same analysis as proposed in refs.[40,41,42]; and based on the results from refs.[40,43,44,45,82] we assume fcc crystalline structures. Using all this information, we make the following assumptions for the vibrational exciton calculations presented in Figs. 8a and 10a (see also section 3.2) : i) The relative abundance of different cluster sizes are taken from the experimental mass spectra. ii) For clusters with $n \leq 50$, the exciton calculations are performed for cluster structures obtained from FF calculations and for $n \leq 38$ from FF calculations with subsequent optimization by DFT, iii) For clusters with $n \gtrsim 50$, we use fcc cuboctahedral structures for the exciton calculations. Based on the additional knowledge on cluster size, abundances, shape and internal structure, this is the best assumption we can make at this point, and to the best of our knowledge also the most detailed compared with previous infrared simulations of CO_2 clusters.

Fig. 8 shows results for the cluster size range $< n >\sim$ 20-60 ($n_{\max} \sim$ 70-190); i. e. the range where the transition to fcc cuboctahedral structures takes place. Panel a contains the experimental (black lines) and the calculated (red lines) infrared spectra together with an experimental CO_2 gas phase spectrum (top trace). The comparison of

the experimental spectra with the gas phase spectrum reveals a very high gas phase contribution in the cluster spectra, which decreases with increasing cluster size. The major gas phase contributions (bands around 2380 cm^{-1}, 2350 cm^{-1} and 2320 cm^{-1}) are labeled with black arrows in the cluster spectrum with $< n >= 21$. We have tried to subtract gas phase spectra from the cluster spectra to compensate gas phase contributions and retrieve pure cluster spectra. However, this was not successful because of the the low S/N ratio of the spectra and the limited spectral resolution (1.5 cm^{-1}). Nevertheless, cluster features are visible in the spectra in agreement with the predictions from exciton calculations (red spectra). The clearest cluster feature in the experimental spectra is a peak at $\sim$ 2361 cm^{-1}, which is labeled with a red arrow in the bottom spectrum. This peak becomes more prominent with increasing cluster size and at the same time shifts by $\sim$ 1 cm^{-1} from $\sim$ 2361 cm^{-1} to $\sim$ 2362 cm^{-1}. The same trend is also seen in the exciton simulations, where the peak at 2359.5 cm^{-1} becomes more prominent and shifts to 2360 cm^{-1} with increasing cluster size. Since these infrared spectra cover the range of the transition to increasingly higher contributions from fcc cuboctahedral structures with increasing cluster size we were wondering whether this prominent peak could originate from fcc cuboctahedral structures. For this purpose we have performed exciton simulations for cuboctahedral clusters of different sizes (see Fig. 9). These spectra indeed show a pronounced peak at $\sim$ 2361 cm^{-1} for clusters with $n \sim$ 55-90, which shifts from 2359 cm^{-1} to 2362 cm^{-1} with increasing size. Since this cluster size range agrees with the average cluster size in the experimental spectra (Fig. 8a) we conclude that the emerging pronounced peak in the experimental infrared spectra is likely a signature of cuboctahedral cluster structures in this size range.

The infrared spectra in Fig. 5 of ref.[34] were recorded at the same temperature ($\sim$ 29 K) as those in Fig. 8a, and were estimated to cover a similar cluster size range ($< n > \leq$ 100). Further above, we have determined a lower bound of $< n > \sim$ 10 for the smallest clusters in ref.[34] (see top trace in Fig. 5). The spectra in Fig. 5 of ref.[34] show indeed similar features as those in Fig. 8a. This holds in particular for the top two spectra in Fig. 5 of ref.[34] compared with the calculated spectrum for $< n >= 21$ in Fig. 8a,

which show similar overall band widths and a main broad band below and an additional pronounced shoulder above 2360 cm^{-1}, respectively. For larger clusters, the shoulder disappears continuously with increasing cluster size in both studies, and the double band structures evolves into a single band around 2360 cm^{-1}. In this size range, however, the overall band widths in Fig. 5 of ref.[34] is larger compared with the present spectra. Since the two different studies were performed at the same temperature in the uniform flows of Laval nozzles this thus hints rather at a difference in the cluster size (distribution) than in the cluster structure. While larger clusters do not show further band broadening (see Fig. 10), a higher contribution of small clusters would explain such a broadening (see e. g. bottom spectra in Fig. 5a). It seems thus plausible that the upper bound of $< n >=$ 100 for the largest clusters provided for Fig. 5 of ref.[34] was too high, which would not be surprising in view of the fact that this was a very crude estimate that was not based on an independent size determination as in the current study.

Fig. 10 covers the next higher cluster size range from $< n >\sim$ 40-330 ($n_{\max} \sim$ 110-710). Again, the spectra of the smaller clusters - in particular that for $< n >= 41$ in panel a - are dominated by gas phase contributions (see black arrows and the pure gas phase spectrum Fig. 8a). For the larger clusters ($< n > \geq 138$), however, the gas phase does no longer dominate and the cluster contribution (broad band around 2360 cm^{-1}) is clearly visible in the spectra in Fig. 10a, in particular when compared with the exciton simulations (see red spectra in panel a). Furthermore, the S/N ratio in the experimental spectra is now high enough to retrieve decent difference spectra, which was not the case in Figs. 4 and 8. Instead of subtracting the gas phase spectrum (top spectrum in panel a) from the experimental spectra we choose to subtract the experimental spectrum recorded for $< n >= 41$ from the other experimental spectra for two reasons: i) We found the subtraction of the pure gas phase spectrum to provide worse results compared with the subtraction of a small cluster spectrum. This is likely due to the fact that the expansion conditions must be slightly varied when measuring pure gas phase for which cluster formation must be avoided. ii) The subtraction of a small cluster spectrum removes contributions from the cluster size range where fcc cuboctahedral clusters do not yet

dominate and thus allows us to clarify at which size the fcc cuboctahedral features start to dominate. The resulting experimental difference spectra (black lines) are shown in Fig. 10b together with exciton simulations for these difference spectra (red lines). The comparison between experiment and simulations shows good agreement, in particular also with respect to the overall band width. It shows that the disagreement of the band width between experiment and simulation in panel a is mainly a consequence of the uncompensated gas phase.

The comparison of the exciton calculations in panels a and b of Fig. 10 shows that the full calculations and the ones for the difference spectra look very similar for the same $< n >$. Above an average cluster sizes of $< n > \sim 217$, they are even identical. This shows that the features from the larger clusters in the size distributions completely dominate these infrared spectra, while the contribution from smaller clusters completely vanishes. Not surprisingly, a comparison with Fig. 9 shows that these spectra are dominated by cuboctahedral features. The simulations for cuboctahedra in this figure shows that the spectral region between $\sim$ 2355-2365 cm^{-1} is dominated by a single band for $n \sim$ 55-90 (see above) and by a double band for $n > 90$. Even though the spectra in Figs. 10a and b are sum spectra over different cluster sizes, this double band is still visible in the exciton spectra. Also visible is the systematic decrease of the relative intensity of the band at the higher wavenumber with increasing cluster size, in agreement with the simulations in Fig. 9. In the experimental difference spectra (Fig. 10b), the double band structure is not so clearly visible. However, the asymmetric band shape at wavenumbers higher than $\sim 2360\,\mathrm{cm}^{-1}$ is consistent with the double band structure.

4.3 Large clusters

Using higher CO_2 concentrations, we were able to record infrared in combination with mass spectra for even larger clusters. The largest cluster size we were able to detect was on the order of $n_{\mathrm{max}} \sim 4300$, which would correspond to a cluster radius of $\sim 3.5\,\mathrm{nm}$ assuming a spherical shape. These sizes are comparable to the lower cluster size range that can also be reached in collisional cooling cell experiments[18,19,21,34]. This is a range

in which a comparison between different cluster generation methods (e. g. collisional cooling with Laval expansions) is in principle possible as demonstrated in ref.[34]. A series of infrared spectra recorded in the uniform Laval expansion for the size range $< n >\sim$ 140-760 ($n_{\max} \sim$ 730-4300) is shown in Fig. 11. In comparison with the previous cases, the gas phase contribution to these spectra is comparatively small (see top spectrum), so that these spectra are dominated by cluster features and not by the gas phase. The double band structure (main band at about 2360 cm^{-1} and a shoulder at about 2364 cm^{-1}) described in Fig. 10 is maintained also for the largest clusters (see also exciton simulations in Fig. 11a). Consistent with the decreasing relative intensity of the shoulder in the exciton spectra with increasing cluster size, the experimental spectra show less structure and a less asymmetric band at wavenumbers higher than $\sim$2360 cm^{-1}. Based on the same arguments as in the previous chapter, we conclude that the infrared spectra of these larger clusters are also dominated by features arising from fcc cuboctahedral clusters.

In Fig. 3a in ref.[34], Bonnamy et al. reported infrared spectra of clusters in a similar size range as our Fig. 11. Over the whole size range from $< n >\sim$ 100-10000, they observed an almost identical single band with an almost perfect symmetric band shape, which only showed a minor shift of the maximum and a slight narrowing of the band with increasing cluster size. These spectra best match the bottom spectrum in our Fig. 11a with $n_{\max} \sim$ 4300, while the structureless symmetric band shape in ref.[34] is not really consistent with our spectra in Fig. 11a for smaller clusters. A major difference between the present study and ref.[34] is the lack of an independent accurate size determination in the latter study. A possible explanation could thus be that the average size indicated in Fig. 3a of ref.[34,39] was not correct for the smaller clusters, and that these smallest cluster had in fact already average size of more that a few thousand molecules (instead of only hundreds of molecules). This would also explain the almost identical symmetric band shape observed for these spectra in ref.[34].

5 Summary

We present a common infrared spectroscopic and mass spectrometric investigation of CO_2 clusters generated in pulsed Laval expansions over the average cluster size range from $< n > \sim$ 3-760 (maximum cluster size $n_{\max} \sim$ 5-4300). To the best of our knowledge, this is the first study that simultaneously uses infrared spectroscopy and mass spectrometry for cluster characterization in this size range. Cluster formation in a Laval expansion allows us to cover a broad cluster size range, and by using the uniform postnozzle flow to investigate clusters at known well defined temperatures. A pulsed Laval expansion is required to keep the pressure in the mass spectrometer low enough for sensitive mass spectrometric studies. However, the disadvantage of the pulsed Laval expansions compared with continuous Laval expansions[34,39] is the limitation it poses on the spectral resolution of the infared spectra. With our rapid scan infrared spectrometer, we are limited to a resolution of $\sim 1.5\,\mathrm{cm}^{-1}$, which makes subtraction of gas phase contributions in the cluster spectra very challenging.

Mass spectra provide detailed information on the whole cluster size distribution; i. e. the relative abundance of different clusters and the number of molecules in the clusters. This independent size information is used to simulate infrared spectra, which are then compared with experimental infrared spectra. Furthermore, through magic clusters the mass spectra also provide additional information on preferred cluster structures. Consistent with previous studies, the preferred structure for CO_2 clusters with $n \gtrsim 50$ is fcc cuboctahedral. The comparison of calculated and experimental infrared spectra reveals that cluster size distributions with average sizes $< n >$ of a few ten molecules show a characteristic band around $2360\,\mathrm{cm}^{-1}$ that originates from the larger clusters in the distribution with fcc cuboctahedral structures. For average sizes that exceed the range $< n > \sim$ 140-220, the infrared spectra are completely dominated by the features of fcc cuboctahedral clusters. Even though we find generally good agreement between simulated and experimental infrared spectra the bands in the experimental spectra tend to be broader compared with the simulations. Uncompensated gas phase contributions are likely one reason for this. Note that the gas phase spectra are not resolved due to our

low spectral resolution. Another reasons might include contributions from other crystal structures (not fcc) or from surface molecules[29,44,84,85,86], which could become considerable when the ratio of surface to core molecules lies close to one[25,34,87,88].

We were not able to record infrared spectra during the very first steps of nucleation/condensation where the average cluster sizes contain only a few molecules because the number concentration of these nucleation clusters was too low and the gas phase fraction too high. However, because of its higher sensitivity we could record mass spectra under these conditions, which at least allows us to calculate infrared spectra for experimental size distributions. These vibrational exciton calculations - based on experimental mass spectra and cluster structures from force field and DFT optimization - predict a pronounced broadening by a factor of about four when the average cluster sizes exceeds $< n > \sim 5$ as a consequence of the increasing number of cluster sizes with different infrared spectra that contribute to the overall spectrum. From an analysis of the mass spectra, we have also retrieved the nucleation behavior of CO_2 under these conditions. The barrierless condensation at the very high supersaturation of $\ln S \sim$ 140-160 is fully consistent with previous trends found for other compounds (see Fig. 4 in[47]). In addition, we have also retrieved a nucleation rate for CO_2 of 1-2 $\cdot 10^{15}$ cm^{-3}s^{-1} at this high supersaturation. The general goal behind our studies is to provide more information about nucleation and early growth at a truly molecular level. The extension to infrared spectroscopy in the present contribution has provided valuable additional information on cluster structures in the early growth regime, which cannot be obtained from mass spectra alone.

Supporting Information

In the Supporting Information, we provide the FF parameters for CO_2, the benchmarking of the DFT functional and the Cartesian coordinates of the energetically lowest lying isomers for n = 2-38 and n = 40, 45, and 50. In addition, we give the structures of the CO_2 clusters for n = 2-38 from M06-2X and selected structures for n = 40-600 from the FF calculations, respectively and analogous figures to Fig. 3 for all cluster sizes with n = 2-38.

Acknowledgements

We are very grateful to David Stapfer and Markus Steger from our workshops for their help with the infrared setup. Financial support was provided by the Swiss National Science Foundation (SNF Project No. 200020-172472) and by ETH Zürich.

References

[1] Isenor, M.; Escribano, R.; Preston, T. C.; Signorell, R. Predicting the infrared band profiles for CO_2 cloud particles on Mars. *Icarus* **2013**, *223*, 591–601.

[2] Trainer, M. G.; Tolbert, M. A.; McKay, C. P.; Toon, O. B. Enhanced CO_2 trapping in water ice via atmospheric deposition with relevance to Mars. *Icarus* **2010**, *206*, 707–715.

[3] Nachbar, M.; Duft, D.; Mangan, T. P.; Martin, J. C. G.; Plane, J.; Leisner, T. Laboratory measurements of heterogeneous CO_2 ice nucleation on nanoparticles under conditions relevant to the Martian mesosphere. *J. Geophys. Res.: Planets* **2016**, *121*, 753–769.

[4] Nachbar, M.; Duft, D.; Leisner, T. The vapor pressure over nano-crystalline ice. *Athmos. Chem. Phys.* **2018**, *18*, 3419–3431.

[5] Oliaee, J. N.; Dehghany, M.; Moazzen-Ahmadi, N.; McKellar, A. R. W. Spectroscopic identification of carbon dioxide clusters: $(CO_2)_6$ to $(CO_2)_{13}$. *Phys. Chem. Chem. Phys.* **2011**, *13*, 1297–1300.

[6] Oliaee, J. N.; Dehghany, M.; McKellar, A. R. W.; Moazzen-Ahmadi, N. High resolution infrared spectroscopy of carbon dioxide clusters up to $(CO_2)_{13}$. *J. Chem. Phys.* **2011**, *135*, 044315.

[7] Dehghany, M.; McKellar, A. R. W.; Afshari, M.; Moazzen-Ahmadi, N. High-resolution infrared spectroscopy of carbon dioxide dimers, trimers, and larger clusters. *Mol. Phys.* **2010**, *108*, 2195–2205.

[8] Häber, T. FTIR-spectroscopy of isolated and argon coated $(HBr)_{n\leq 4}$ clusters in supersonic slit-jet expansions. *Phys. Chem. Chem. Phys.* **2003**, *5*, 1365–1369.

[9] Häber, T.; Schmitt, U.; Suhm, M. A. FTIR-spectroscopy of molecular clusters in pulsed supersonic slit-jet expansions. *Phys. Chem. Chem. Phys.* **1999**, *1*, 5573–5582.

[10] Liu, Y.; Weimann, M.; Suhm, M. A. Extension of panoramic cluster jet spectroscopy into the far infrared: low frequency modes of methanol and water clusters. *Phys. Chem. Chem. Phys.* **2004**, *6*, 3315–3319.

[11] Quack, M.; Schmitt, U.; Suhm, M. A. FTIR spectroscopy of hydrogen fluoride clusters in synchronously pulsed supersonic jets. Isotopic isolation, substitution and 3-d condensation. *Chem. Phys. Lett.* **1997**, *269*, 29–38.

[12] Weimann, M.; Fárník, M.; Suhm, M. A. A first glimpse at the acidic proton vibrations in HCl–water clusters via supersonic jet FTIR spectroscopy. *Phys. Chem. Chem. Phys.* **2002**, *4*, 3933–3937.

[13] Didriche, K.; Lauzin, C.; Macko, P.; Lafferty, W. J.; Saykally, R. J.; Herman, M. On the role of molecular clustering on infrared absorption line shapes of acetylene in a supersonic expansion. *Chem. Phys. Lett.* **2008**, *463*, 345–348.

[14] Bush, M. F. and Saykally, R. J. and Williams, E. R. Infrared action spectra of Ca^{2+} $(H_2O)_{11-69}$ exhibit spectral signatures for condensed-phase structures with increasing cluster size. *J. Am. Chem. Soc.* **2008**, *130*, 15482–15489.

[15] Weida, M. J.; Nesbitt, D. J. Geometric isomerism in clusters: high resolution infrared spectroscopy of a noncyclic CO_2 trimer. *J. Chem. Phys.* **1996**, *105*, 10210–10223.

[16] Steinbach, C.; Buck, U. Vibrational spectroscopy of size-selected sodium-doped water clusters. *J. Phys. Chem. A* **2006**, *110*, 3128–3131.

[17] Pradzynski, C. C.; Dierking, C. W.; Zurheide, F.; Forck, R. M.; Buck, U.; Zeuch, T.; Xantheas, S. S. Infrared detection of $(H_2O)_{20}$ isomers of exceptional stability: a drop-like and a face-sharing pentagonal prism cluster. *Phys. Chem. Chem. Phys.* **2014**, *16*, 26691–26696.

[18] Lang, K. E.; Knox, K. J.; Momose, T.; Signorell, R. Infrared spectroscopy and phase behavior of n-butane aerosols and thin films at cryogenic temperatures. *J. Phys. Chem. A* **2013**, *117*, 11745–11759.

612 [19] Lang, K. E.; Knox, K. J.; Signorell, R. Phase behavior of propane and n-pentane
613 aerosol particles under conditions relevant to Titan. *Planet. Space Sci.* **2013**, *75*,
614 56–68.

615 [20] Kunzmann, M. K.; Signorell, R.; Taraschewski, M. ; Bauerecker, S. The formation
616 of N_2O nanoparticles in a collisional cooling cell between 4 and 110 K. *Phys. Chem.*
617 *Chem. Phys.* **2001**, *3*, 3742–3749.

618 [21] Disselkamp, R.; Ewing, G. E. Large CO_2 clusters studied by infrared spectroscopy
619 and light scattering. *Phys. Chem. Chem. Phys.* **1993**, *99*, 2439–2448.

620 [22] Firanescu, G.; Luckhaus, D.; Signorell, R. Phase, shape, and architecture of SF_6 and
621 SF_6/CO_2 aerosol particles: Infrared spectra and modeling of vibrational excitons. *J.*
622 *Chem. Phys.* **2008**, *128*, 184301.

623 [23] Wang, C. C.; Zielke, P.; Sigurbjörnsson, O. F.; Viteri, C. R.; Signorell, R. Infrared
624 spectra of C_2H_6, C_2H_4, C_2H_2, and CO_2 aerosols potentially formed in Titan's atmo-
625 sphere. *J. Phys. Chem. A* **2009**, *113*, 11129–11137.

626 [24] Barnes, J. A.; Gough, T. E. Fourier transform infrared spectroscopy of molecular
627 clusters: The structure and internal mobility of clustered carbon dioxide. *J. Chem.*
628 *Phys.* **1987**, *86*, 6012–6017.

629 [25] Devlin, J. P.; Joyce, C.; Buch, V. Infrared spectra and structures of large water
630 clusters. *J. Phys. Chem. A* **2000**, *104*, 1974–1977.

631 [26] Gough, T. E.; Wang, T. Vibrational spectroscopy of cocrystallized carbon dioxide
632 and acetylene. *J. Chem. Phys.* **1995**, *102*, 3932–3937.

633 [27] Ennis, C.; Auchettl, R.; Ruzi, M.; Robertson, E. G. Infrared characterisation of
634 acetonitrile and propionitrile aerosols under Titan's atmospheric conditions. *Phys.*
635 *Chem. Chem. Phys.* **2017**, *19*, 2915–2925.

636 [28] Baurecker, S.; Taraschewski, M.; Weitkamp, C.; Cammenga, H. K. Liquid-helium

temperature long-path infrared spectroscopy of molecular clusters and supercooled molecules. *Rev. Sci. Instrum.* **2001**, *72*, 3946–3955.

[29] Sigurbjörnsson, O. F.; Firanescu, G.; Signorell, R. Vibrational exciton coupling as a probe for phase transitions and shape changes of fluoroform aerosol particles. *Phys. Chem. Chem. Phys.* **2009**, *11*, 187–194.

[30] Jetzki, M.; Bonnamy, A.; Signorell, R. Vibrational delocalization in ammonia aerosol particles. *J. Chem. Phys.* **2004**, *120*, 11775–11784.

[31] Signorell, R. Verification of the vibrational exciton approach for CO_2 and N_2O nanoparticles. *J. Chem. Phys.* **2003**, *118*, 2707–2715.

[32] *Fundamentals and Applications in Aerosol Spectroscopy.* Signorell, R.; Reid, J. P.; CRC Press, Boca Raton, 2010.

[33] Tanimura, S.; Okada, Y.; Takeuchi, K. FTIR spectroscopy of UF_6 clustering in a supersonic Laval nozzle. *J. Phys. Chem.* **1996**, *100*, 2842–2848.

[34] Bonnamy, A.; Georges, R.; Hugo, E.; Signorell, R. IR signature of $(CO_2)_N$ clusters: size, shape and structural effects. *Phys. Chem. Chem. Phys.* **2005**, *7*, 963–969.

[35] Laksmono, H.; Tanimura, S.; Allen, H. C.; Wilemski, G.; Zahniser, M. S.; Shorter, J. H.; Nelson, D. D.; McManus, J. B.; Wyslouzil, B. E. Monomer, clusters, liquid: an integrated spectroscopic study of methanol condensation. *Phys. Chem. Chem. Phys.* **2011**, *13*, 5855–5871.

[36] Manka, A.; Pathak, H.; Tanimura, S.; Wölk, J.; Strey, R.; Wyslouzil, B. E. Freezing water in no-man's land. *Phys. Chem. Chem. Phys.* **2012**, *14*, 4505–4516.

[37] Modak, V. P.; Pathak, H.; Thayer, M.; Singer, S. J.; Wyslouzil, B. E. Experimental evidence for surface freezing in supercooled *n*-alkane nanodroplets. *Phys. Chem. Chem. Phys.* **2013**, *15*, 6783–6795.

[38] Amaya, A. J.; Wyslouzil, B. E. Ice nucleation rates near ∼225 K. *J. Chem. Phys.* **2018**, *148*, 084501.

[39] Bonnamy, A.; Georges, R.; Benidar, A.; Boissoles, J.; Canosa, A.; Rowe, B. R. Infrared spectroscopy of $(CO_2)_N$ nanoparticles (30<N<14500) flowing in a uniform supersonic expansion. *J. Chem. Phys.* **2003**, *118*, 3612–3621.

[40] Negishi, Y.; Nagata, T.; Tsukuda, T. Structural evolution in $(CO_2)_n$ clusters ($n < 10^3$) as studied by mass spectrometry. *Chem. Phys. Lett.* **2002**, *364*, 127–132.

[41] Ingolfsson, O.; Wodtke, A. M. Electron attachment time-of-flight mass spectrometry reveals geometrical shell closings in van der Waals aggregates. *J. Chem. Phys.* **2002**, *117*, 3721–3732.

[42] Näher, U.; Zimmermann, U.; Martin, T. P. Geometrical shell structure of clusters. *J. Chem. Phys.* **1993**, *99*, 2256–2260.

[43] Torchet, G.; de Feraudy, M.-F.; Boutin, A.; Fuchs, A. H. Structural transformation in $(CO_2)_N$ clusters, N<100. *J. Chem. Phys.* **1996**, *105*, 3671–3678.

[44] Maillet, J.-B.; Boutin, A.; Fuchs, A. H. From molecular clusters to bulk matter. II. Crossover from icosahedral to crystalline structures in CO_2 clusters. *J. Chem. Phys.* **1999**, *111*, 2095–2102.

[45] Liu, H.; Jordan, K. D. Finite Temperature Properties of $(CO_2)_n$ Clusters. *J. Phys. Chem. A* **2003**, *107*, 5703–5709.

[46] Signorell, R.; Jetzki, M.; Kunzmann, RM.; Ueberschaer, R. Unraveling the origin of band shapes in infrared spectra of N_2O-$^{12}CO_2$ and $^{12}CO_2$-$^{13}CO_2$ ice particles. *J. Phys. Chem. A* **2006**, *110*, 2890–2897.

[47] Lippe, M.; Chakrabarty, S.; Ferreiro, J. J.; Tanaka, K. K.; Signorell, R. Water nucleation at extreme supersaturation. *J. Chem. Phys.* **2018**, *149*, 244303.

[48] Chakrabarty, S.; Ferreiro, J. J.; Lippe, M.; Signorell, R. Toluene cluster formation in Laval expansions: nucleation and growth. *J. Phys. Chem. A* **2017**, *121*, 3991-4001.

[49] Ferreiro, J. J.; Chakrabarty, S.; Schläppi, B.; Signorell, R. Observation of propane cluster size distributions during nucleation and growth in a Laval expansion. *J. Chem. Phys.* **2016**, *145*, 211907.

[50] Schläppi, B.; Litman, J. H.; Ferreiro, J. J.; Stapfer, D.; Signorell, R. A pulsed uniform Laval expansion coupled with single photon ionization and mass spectrometric detection for the study of large molecular aggregates. *Phys. Chem. Chem. Phys.* **2015**, *17*, 25761–25771.

[51] Ferreiro, J. J.; Gartmann, T. E.; Schläppi, B.; Signorell, R. Can we observe gas phase nucleation at the molecular level? *Z. Phys. Chem.* **2015**, *229*, 1765-1780.

[52] Atkinson, D. B.; Smith, M. A. Design and characterization of pulsed uniform supersonic expansions for chemical applications. *Rev. Sci. Instrum.* **1995**, *66*, 4434–4446.

[53] Forysinski, P. W.; Zielke, P.; Luckhaus, D.; Signorell, R. PFI-ZEKE photoelectron spectrum of CH_2F_2, ionisation potential and ionic fragmentation appearance potentials. *Phys. Chem. Chem. Phys.* **2010**, *12*, 3121-3130.

[54] Yoder, B. L.; Litman, J. H.; Forysinski, P. W.; Corbett, J. L.; Signorell, R. Sizer for neutral weakly bound ultrafine aerosol particles based on sodium doping and mass spectrometric detection. *J. Phys. Chem. Lett.* **2011**, *2*, 2623–2628.

[55] Litman, J. H.; Yoder, B. L.; Schläppi, B.; Signorell, R. Sodium-doping as a reference to study the influence of intracluster chemistry on the fragmentation of weakly-bound clusters upon vacuum ultraviolet photoionization. *Phys. Chem. Chem. Phys.* **2013**, *15*, 940-949.

[56] Heinbuch, S.; Dong, F.; Rocca, J. J.; Bernstein, E. R. Single photon ionization of van der Waals clusters with a soft x-ray laser: $(CO_2)_n$ and $(CO_2)_n(H_2O)_m$. *J. Chem. Phys.* **2006**, *125*, 154316.

[57] Fárník, M.; Lengyel, J. Mass spectrometry of aerosol particle analogues in molecular beam experiments. *Mass Spectrom. Rev.* **2018**, *37*, 630–651.

[58] Pysanenko, A.; Lengyel, J.; Fárník, M. Uptake of methanol on mixed HNO_3/H_2O clusters: An absolute pickup cross section. *Mass Spectrom. Rev.* **2018**, *148*, 154301.

[59] Wang, L. S.; Reutt, J. E.; Lee, Y. T.; Shirley, D. A. High resolution UV photoelectron spectroscopy of CO^+_2, COS^+ and CS^+_2 using supersonic molecular beams. *J. Electron Spectrosc. Relat. Phenom.* **1988**, *47*, 167–186.

[60] Zhang, J.; Dolg, M. ABCluster: the artificial bee colony algorithm for cluster global optimization. *Phys. Chem. Chem. Phys.* **2015**, *17*, 24173–24181.

[61] Zhang, J.; Dolg, M. Global optimization of clusters of rigid molecules using the artificial bee colony algorithm. *Phys. Chem. Chem. Phys.* **2016**, *18*, 3003–3010.

[62] MacKerell, A. D.; Bashford, D.; Bellott, M.; Dunbrack, R. L.; Evanseck, J. D.; Field, M. J.; Fischer, S.; Gao, J.; Guo, H.; Ha, S.; et al. All-atom empirical potential for molecular modeling and dynamics studies of proteins. *J. Phys. Chem. B* **1998**, *102*, 3586-3616.

[63] Frisch, M. J.; Trucks, G. W.; Schlegel, H. B.; Scuseria, G. E.; Robb, M. A.; Cheeseman, J. R.; Scalmani, G.; Barone, V. ; Mennucci, B.; Petersson, G. A.; et al. *Gaussian 09, revision A. 1* Gaussian Inc. Wallingford CT 27, 2009.

[64] Becke, A. D. Density-functional thermochemistry. III. The role of exact exchange. *J. Chem. Phys.* **1993**, *98*, 5648–5652.

[65] Lee, C.; Yang, W.; Parr, R. G. Development of the Colle-Salvetti correlation-energy formula into a functional of the electron density. *Phys. Rev. B* **1988**, *37*, 785–789.

[66] Stephens, P. J.; Devlin, F. J.; Chabalowski, C. F.; Frisch, M. J. Ab initio calculation of vibrational absorption and circular dichroism spectra using density functional force fields. *J. Phys. Chem.* **1994**, *98*, 11623–11627.

[67] Schwabe, T.; Grimme, S. Double-hybrid density functionals with long-range dispersion corrections: higher accuracy and extended applicability. *Phys. Chem. Chem. Phys.* **2007**, *9*, 3397–3406.

[68] Zhao, Y.; Truhlar, D. G. The M06 suite of density functionals for main group thermochemistry, thermochemical kinetics, noncovalent interactions, excited states, and transition elements: two new functionals and systematic testing of four M06-class functionals and 12 other functionals. *Theor. Chem. Acc.* **2008**, *120*, 215–241.

[69] Dill, J. D.; Pople, J. A. Self-consistent molecular orbital methods. XV. Extended Gaussian-type basis sets for lithium, beryllium, and boron. *J. Chem. Phys.* **1975**, *62*, 2921–2923.

[70] Lemke, K. H.; Seward, T. M. Thermodynamic properties of carbon dioxide clusters by M06-2X and dispersion-corrected B2PLYP-D theory. *Chem. Phys. Lett.* **2013**, *573*, 19–23.

[71] Xie, X.; Wu, C.; Liu, Y.; Huang, W.; Deng, Y.; Liu, Y.; Gong, Q.; Wu, C. Identifying isomers of carbon-dioxide clusters by laser-driven Coulomb explosion. *Phys. Rev. A* **2014**, *90*, 033411.

[72] Takeuchi, H. Geometry optimization of carbon dioxide clusters $(CO_2)_n$ for $4 \leq n \leq 40$. *J. Phys. Chem. A* **2008**, *112*, 7492–7497.

[73] Herzberg, G. *Molecular Spectra and Molecular Structure. Vol. 3: Electronic Spectra and Electronic Structure of Polyatomic Molecules.* Van Nostrand Reinhold, New York, 1966.

[74] Shimanouchi, T. *Tables of Molecular Vibrational Frequencies.* National Bureau of Standards, Washington D. C., 1980.

[75] Weida, M. J.; Sperhac, J. M.; Nesbitt, D. J. High-resolution infrared diode laser spectroscopy of $(CO_2)_3$: Vibrationally averaged structures, resonant dipole vibrational shifts, and tests of CO_2–CO_2 pair potentials. *J. Chem. Phys.* **1995**, *103*, 7685–7699.

[76] Jucks, K. W.; Huang, Z. S.; Miller, R. E.; Fraser, G. T.; Pine, A. S.; Lafferty, W. J. Structure and vibrational dynamics of the CO_2 dimer from the sub-Doppler infrared spectrum of the 2.7 μm Fermi diad. *J. Chem. Phys.* **1988**, *88*, 2185–2195.

[77] Fraser, G. T.; Pine, A. S.; Lafferty, W. J.; Miller, R. E. Sub-Doppler infrared spectrum of the carbon dioxide trimer. *J. Chem. Phys.* **1987**, *87*, 1502–1508.

[78] Walsh, M. A.; England, T. H.; Dyke, T. R.; Howard, B. J. Pulsed molecular beam infrared absorption spectroscopy of CO_2 dimer. *Chem. Phys. Lett.* **1987**, *142*, 265–270.

[79] Signorell, R. Infrared spectroscopy of particulate matter: between molecular clusters and bulk. *Mol. Phys.* **2003**, *101*, 3385-3399.

[80] Rothman, L. S.; Benedict, W. S. Infrared energy levels and intensities of carbon dioxide. *Appl. Opt.* **1978**, *17*, 2605–2611.

[81] Bonnamy, A.; Jetzki, M; Signorell, R. Optical properties of molecular ice particles from a microscopic model. *Chem. Phys. Lett.* **2003**, *382*, 547–552.

[82] Torchet, G.; Bouchier, H.; Farges, J.; De Feraudy, M. F.; Raoult, B. Size effects in the structure and dynamics of CO_2 clusters. *J. Chem. Phys.* **1984**, *81*, 2137–2143.

[83] Duff, K. M. Non-equilibrium condensation of carbon dioxide in supersonic nozzles. Ph.D. Dissertation, Massachusetts Institute of Technology, Cambridge, MA, 1966.

[84] Cardini, G.; Schettino, V.; Klein, M. L. Structure and dynamics of carbon dioxide clusters: a molecular dynamics study. *J. Chem. Phys.* **1989**, *90*, 4441–4449.

[85] Maillet, J.-B.; Boutin, A.; Buttefey, S.; Calvo, F.; Fuchs, A. H. From molecular clusters to bulk matter. I. Structure and thermodynamics of small CO_2, N_2, and SF_6 clusters. *J. Chem. Phys.* **1998**, *109*, 329–337.

[86] Murthy, C. S.; O'Shea, S. F.; McDonald, I. R. Electrostatic interactions in molecular crystals: lattice dynamics of solid nitrogen and carbon dioxide. *Mol. Phys.* **1983**, *50*, 531–541.

[87] Häber, T.; Schmitt, U.; Emmeluth, C.; Suhm, M. A. Ragout-jet FTIR spectroscopy of cluster isomerism and cluster dynamics: from carboxylic acid dimers to N_2O nanoparticles. *Faraday Discuss.* **2001**, *118*, 331–359.

[88] Kunzmann, M. K.; Bauerecker, S.; Suhm, M. A.; Signorell, R. Spectroscopic characterization of N_2O aggregates: from clusters to the particulate state. *Spectrochim. Acta A* **2003**, *59*, 2855–2865.

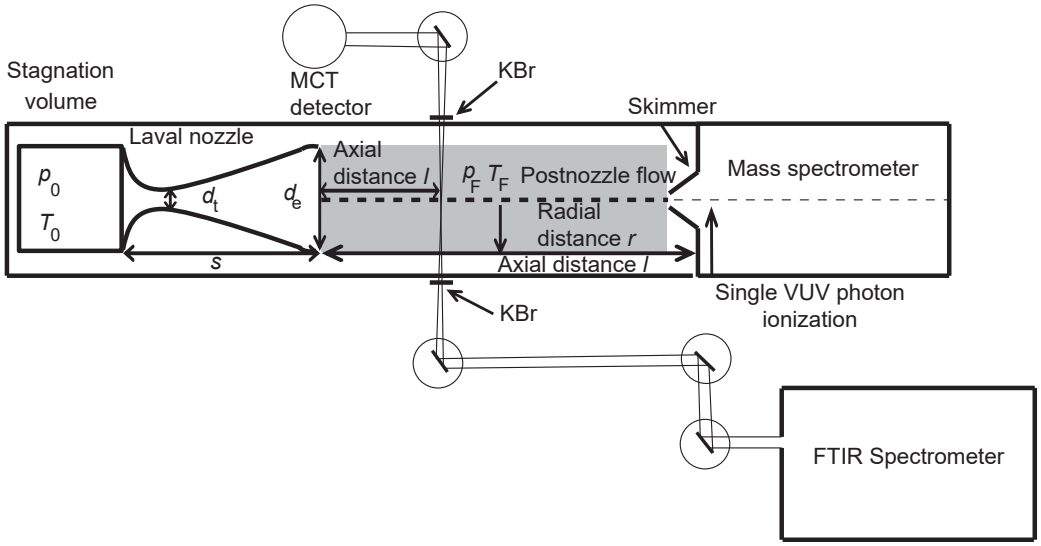

Figure 1: Schematic of the experimental setup [49,48]. p_0, T_0, p_F and T_F are the stagnation pressure, the stagnation temperature, the flow pressure, and the flow temperature, respectively. d_t, d_e, and s is the throat diameter, the exit diameter, and the length of the Laval nozzle, respectively. r is the radial distance from the center of the expansion. The axial distance l is the distance between the nozzle exit and the skimmer. l can be varied, which corresponds to a variation in the growth time t. The central part of the expansion is sampled into the mass spectrometer by a skimmer, where the clusters are ionized and detected. FTIR measurements were performed in the postnozzle flow of the Laval expansion in positions corresponding to the same axial distance as measured with mass spectrometry.

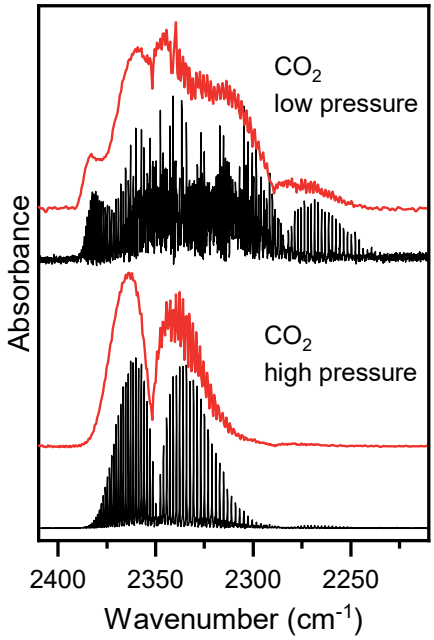

Figure 2: Top: Infrared spectrum of CO_2 at low pressure ($< 1\,\mathrm{mbar}$) measured with high (black, $0.25\,\mathrm{cm}^{-1}$) and low (red, $1.5\,\mathrm{cm}^{-1}$) resolution. Bottom: Infrared spectrum of CO_2 at a pressure of about 1 bar measured with high (black, $0.25\,\mathrm{cm}^{-1}$) and low (red, $1.5\,\mathrm{cm}^{-1}$) resolution. The pressure was increased by addition of argon gas. All spectra were measured at room temperature.

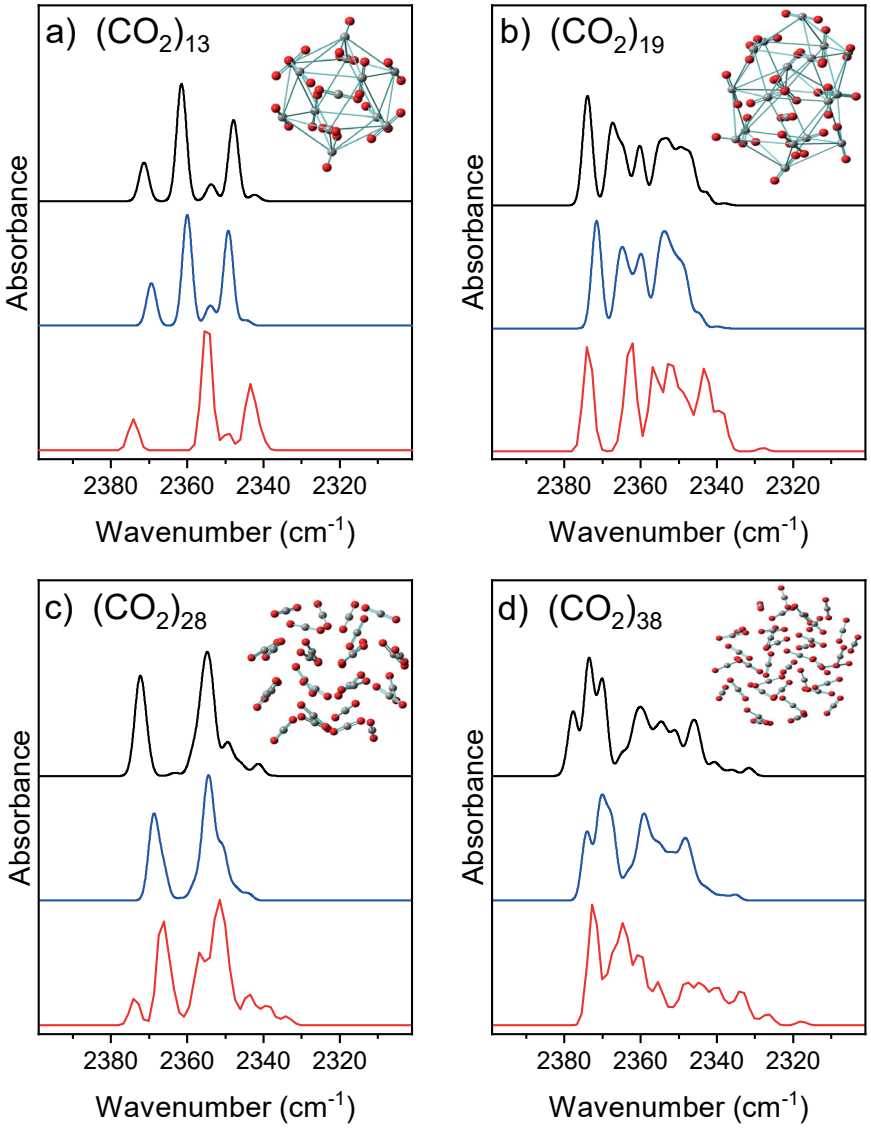

Figure 3: Simulated infrared spectra of the most stable structures of $(CO_2)_n$ (n = 13 (a), 19 (b), 28 (c), and 38 (d)) using Gaussian with optimized M06-2X structures (red, lower), exciton calculations with optimized FF structures (blue, middle), and exciton calculations with optimized M06-2X structures (black, upper) are shown.

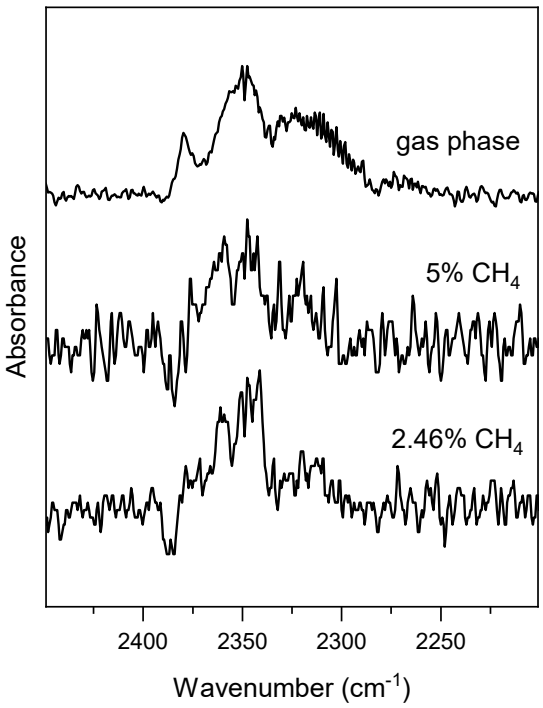

Figure 4: Pure gas phase spectrum (top) and two experimental FTIR spectra under CO_2 nucleation conditions (0.18% CO_2) with 5% (middle) and 2.46% (bottom) methane.

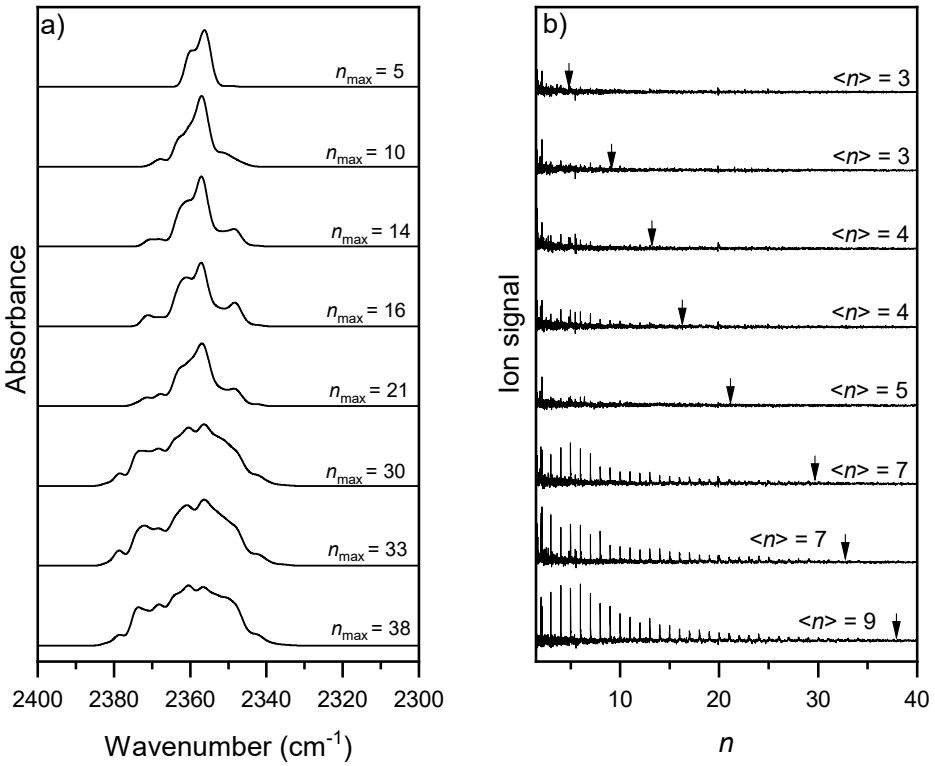

Figure 5: a) Infrared spectra of clusters during nucleation. The spectra are calculated with the exciton model for the cluster size distributions shown in trace b. $n_{\max}$ is indicated in the graph. b) Mass spectra of clusters during nucleation at $\sim 29\,\mathrm{K}$ and 0.18% CO_2 with methane concentrations between 0 and 8.23%. $n_{\max}$ is indicated by arrows (values see trace a) in addition to the values of $< n >$.

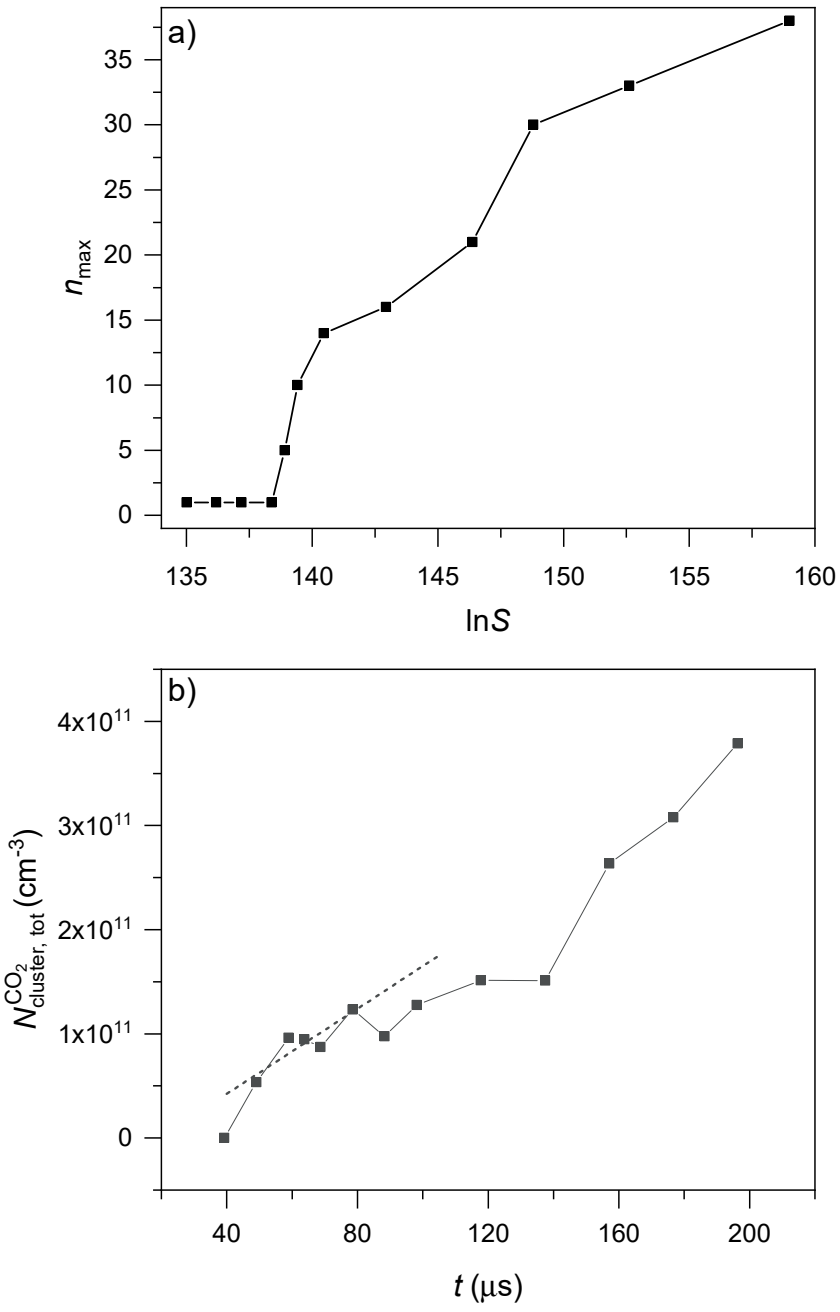

Figure 6: a) $n_{\max}$ from Fig. 5b as a function of ln$S$. The nucleation behavior hints at a barrierless nucleation process which is consistent with the high S value. b) Total cluster number concentration of CO_2 clusters as a function of the nucleation time at constant supersaturation ln$S \sim 160$. The nucleation/condensation rate is determined by a linear fit (see dashed line) and is on the order of 1-2·10^{15} cm^{-3}s^{-1}.

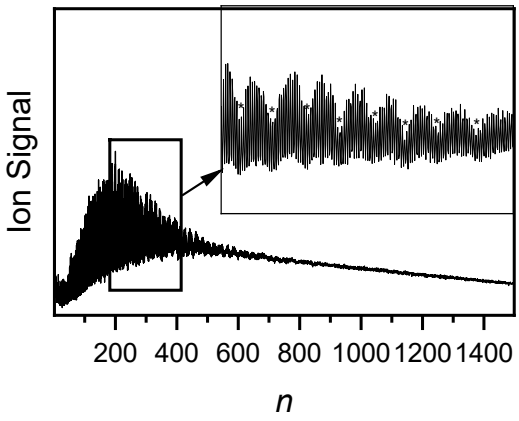

Figure 7: Mass spectrum for 5% CO_2 at $\sim 29\,\mathrm{K}$. The inset shows a zoom-in of the part shown by the rectangle. Local minima of the ion signal for cluster sizes $n \gtrsim 55$ are marked with asterisks, these correspond to shell and subshell closings.

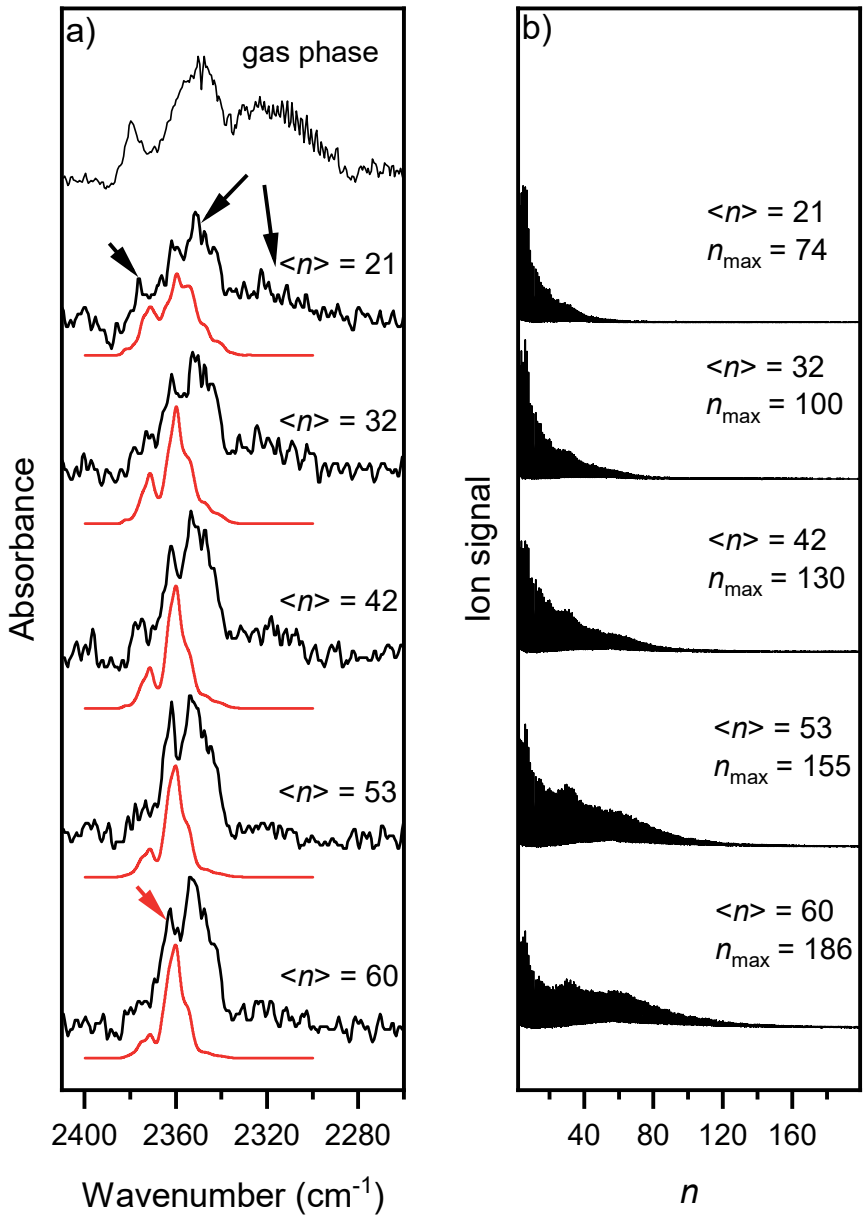

Figure 8: a) Experimental infrared spectra recorded at ~ 29 K for 0.38% CO_2 (black) with respective exciton simulations (red). $< n >$ is indicated for each spectrum. The black arrows in the second top spectrum show where we observe mainly gas phase contributions. The red arrow in the bottom spectrum shows where we observe cluster contributions. A pure gas phase spectrum is shown on top. b) Corresponding mass spectra. $< n >$ and $n_{\max}$ are indicated in the figure.

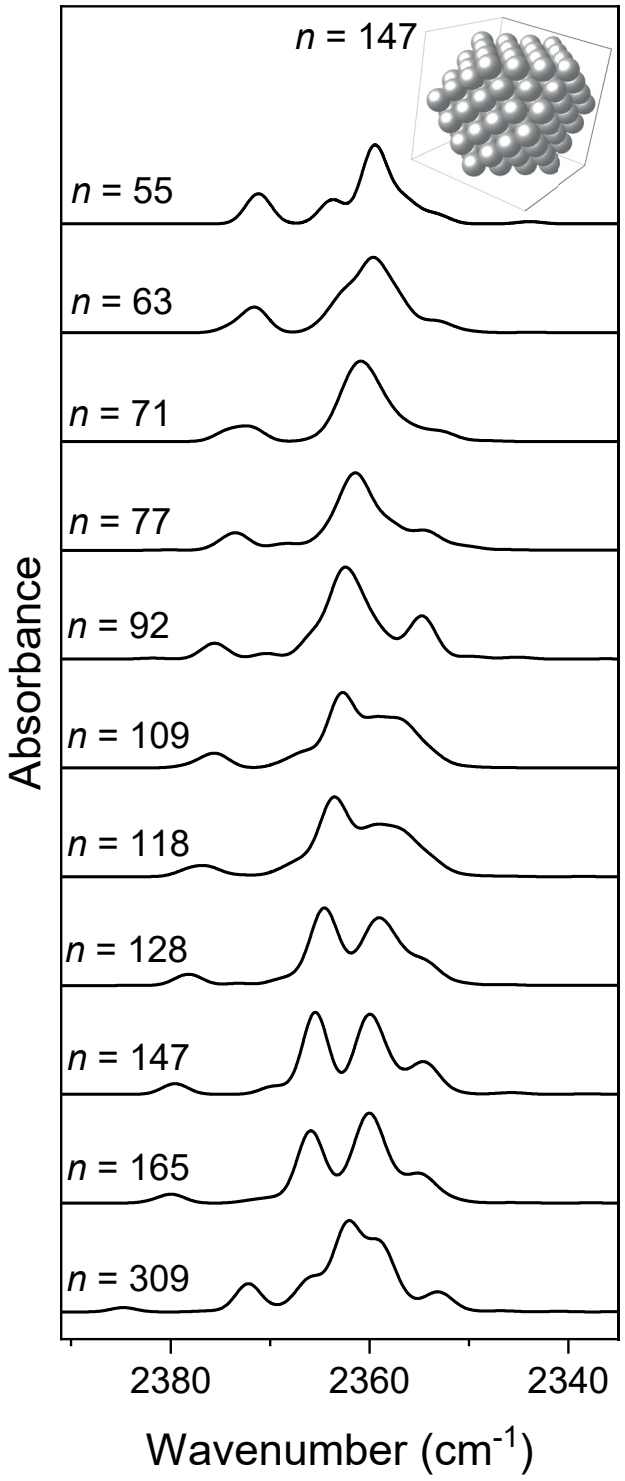

Figure 9: Calculated infrared spectra (exciton calculations) for cuboctahedral structures with n molecules per cluster. A complete shell closed cuboctahedral structure for $n = 147$ is displayed on top of the graph.

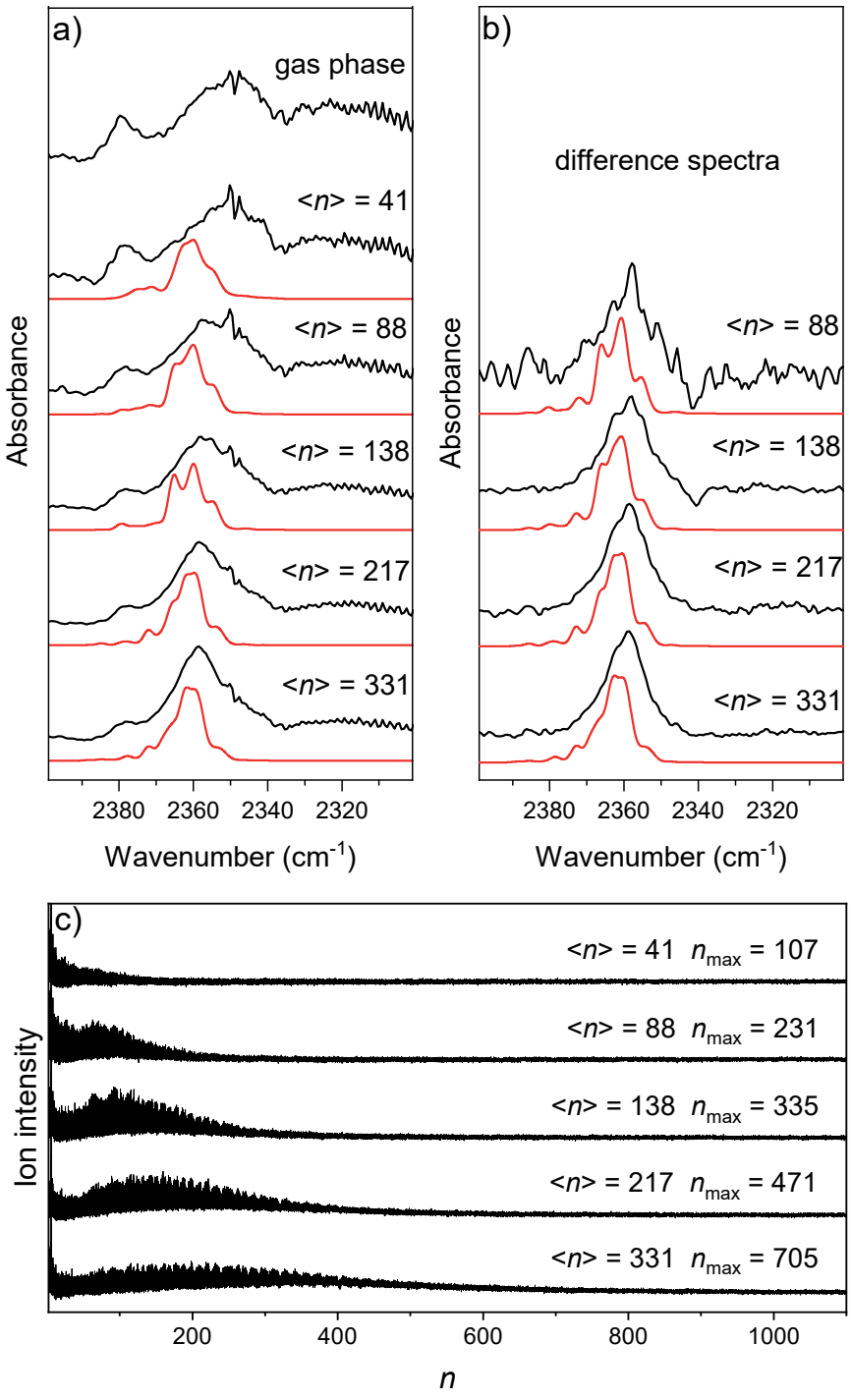

Figure 10: a) Experimental and exciton calculated infrared spectra at $\sim 43\,\mathrm{K}$ for 2.48% CO_2 for different $< n >$ as indicated for each trace. The experimental spectra are shown in black and the exciton calculations in red. A pure gas phase spectrum is shown on top. b) Experimental difference infrared spectra (black) with corresponding difference exciton simulations (red). The difference spectra were obtained by subtracting the cluster spectrum for $< n > = 41$ from the spectra with $< n > = 88$, 138, 217, 331 (see text). c) Corresponding mass spectra.

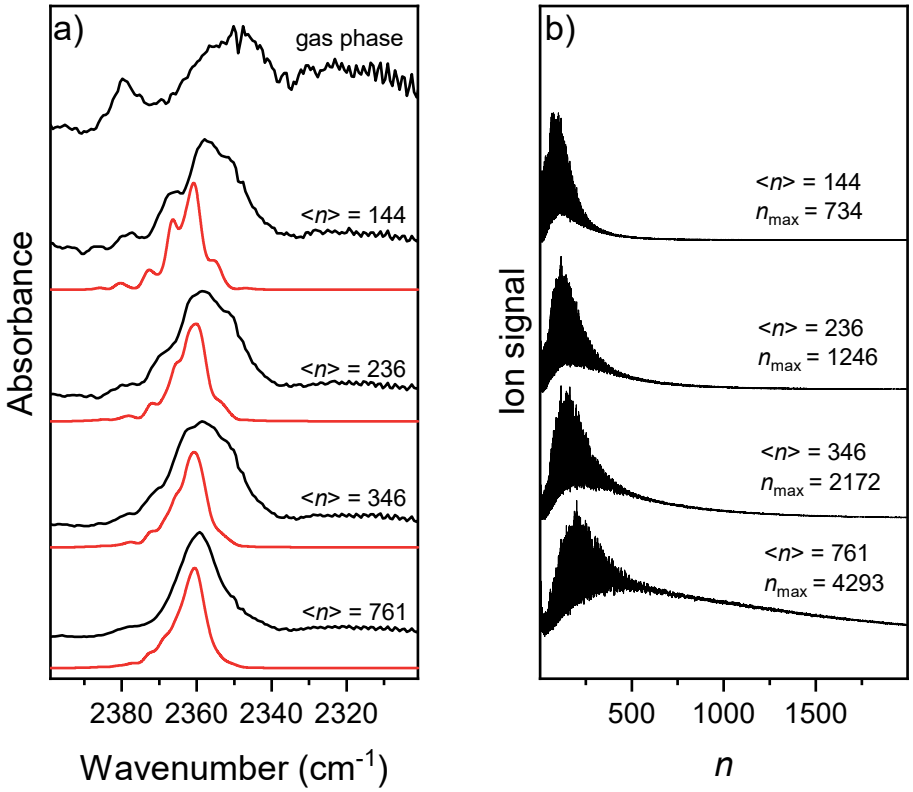

Figure 11: a) Experimental (black) and calculated (red) infrared spectra at $\sim$ 29 K for different concentrations of CO_2 (1, 1.6, 2.3 and 5% from top to bottom). A pure CO_2 gas phase spectrum is shown on top. b) Corresponding mass spectra.

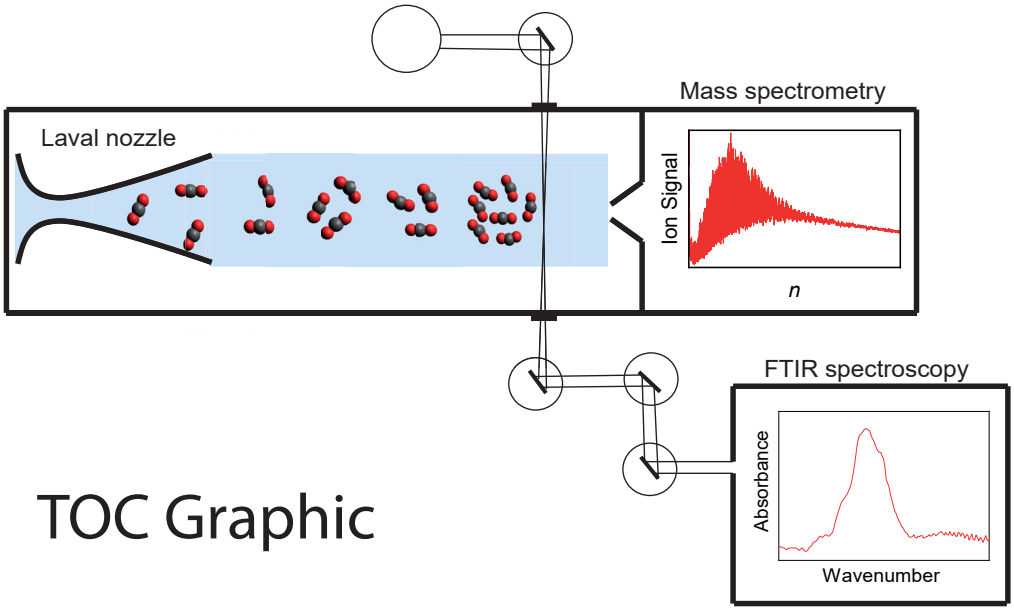
Mass spectrometry
Laval nozzle
Ion Signal
n
FTIR spectroscopy
Absorbance
Wavenumber

TOC Graphic